Check for updates

Advanced Functional Materials

ADVANCED FUNCTIONAL MATERIALS
www.afm-journal.de

RESEARCH ARTICLE OPEN ACCESS

A Mechanistic Blueprint for Fast, High-Yield Green Scintillators Using Conjugated Polymer–Nanocrystal Composites

Chenger Wang[1] | Emanuele Mazzola[2,3] | Andrea Fratelli[1,4] | Matteo L. Zaffalon[1] | Francesco Bruni[1,2] | Francesco Carulli[1] | Xiaohe Zhou[1] | Saptarshi Chakraborty[1] | Leonardo Poletti[5] | Luca Cappelletti[1] | Francesco Meinardi[1] | Francesca Rossi[5] | Luca Gironi[2,3] | Sergio Brovelli[1,2]

[1]Dipartimento di Scienza dei Materiali, Università degli Studi di Milano-Bicocca, Milano, Italy | [2]INFN—Sezione di Milano—Bicocca, Milano, Italy | [3]Dipartimento di Fisica, Università degli Studi di Milano-Bicocca, Milan, Italy | [4]Nanochemistry, Istituto Italiano di Tecnologia, Genova, Italy | [5]IMEM-CNR, Parma, Italy

Correspondence: Chenger Wang (chenger.Wang@unimib.It) | Sergio Brovelli (sergio.brovelli@unimib.It)

Received: 4 December 2025 | **Revised:** 13 February 2026 | **Accepted:** 3 March 2026

ABSTRACT

Nanocrystal-sensitized plastic scintillators offer promise for high-performance radiation detectors, but achieving both high efficiency and ultrafast timing remains challenging. This need grows as the field moves away from blue emitters, whose spectra overlap radio-induced defect bands in polymers, toward green/yellow emitters that avoid these losses. Yet green dyes typically suffer from slow photophysics. Here, we show green-emitting polymer 9,9-dioctylfluorene-alt-benzothiadiazole (F8BT) overcomes this limitation through large Stokes shift and fast emission, making it a compelling scintillator matrix. We use F8BT to clarify sensitization mechanisms in nanocrystal/polymer systems by blending it with non-emissive high-Z HfO_2 nanocrystals (NCs) or emissive CdZnS/ZnS (CZS) quantum dots (QDs) to isolate high-Z and optical sensitization pathways. HfO_2/F8BT films exhibit 25× radioluminescence (RL) enhancement but decreasing light yield (LY) with increasing NCs loading, indicating that HfO_2 acts as passive energy-dissipation centers for secondary electrons. Conversely, CZS/F8BT films achieve 70× RL enhancement with loading-independent LY, demonstrating that emissive QDs recycle secondary electrons and enable dual sensitization. Both systems preserve sub-3 ns decay times due to F8BT's ultrafast emission and QD multiexciton dynamics. α-particle detection further confirms practical applicability. These findings establish a scalable blueprint for fast, efficient, green-emitting scintillators that circumvent defect-band absorption while enabling mechanistically informed dual sensitization.

1 | Introduction

Scintillators are critical components in a wide range of radiation detection technologies, including medical imaging, security screening, high-energy physics, and space exploration [1]. Nanomaterial-based scintillators have recently emerged as promising candidates for next-generation radiation detection [2, 3]. This is due to their advantages in material design flexibility [4], scalable chemical synthesis [5–7], high emission yield, ultrafast decay time [8–10], high atomic number (Z), defect tolerance [11], and radiation hardness [12]. Embedding inorganic nanocrystals (NCs) into organic matrices (solutions or polymers) to prepare hybrid or composite scintillators that combine the advantages of both inorganic and organic materials represents the primary application method for nanomaterials in radiation detection. The modification of traditional plastic scintillators through heavy metal doping to meet the requirements of gamma spectroscopy has driven research into high-Z NCs sensitized scintillators

This is an open access article under the terms of the Creative Commons Attribution License, which permits use, distribution and reproduction in any medium, provided the original work is properly cited.

© 2026 The Author(s). *Advanced Functional Materials* published by Wiley-VCH GmbH

[13]. Among these, wide-bandgap non-emissive particles such as Gd_2O_3 [14], HfO_2 [15, 16], and YbF_3 [17]. NCs are selected as high-Z sensitizers, converting gamma ray into photoelectrons, thereby sensitizing organic dyes (so-called high-Z sensitization) [13]. Since this sensitization process is based on the essentially instantaneous release and recapture of photoelectrons and does not participate in the luminescence process of the emitter, it has become an effective strategy for designing fast composite scintillators that leverage the excitonic luminescence of organic dyes [18, 19]. Semiconductor NCs quantum dots (QDs), like II-VI QDs and perovskite QDs, have also been widely studied for scintillators [20–23], especially prized for their ultrafast multiexcitonic scintillation that enables sub-ns lifetimes [6, 12, 24]. However, the light yield (LY, defined as the number of emitted photons per unit of deposited energy) of QD-based scintillators as the sole phosphor faces challenges due to the trade-off between self-absorption and high loading [25–27]. Constructing energy transfer systems between QDs and organic luminescent materials has the promise of overcoming the limitations of single-QDs systems. In this case, QDs can serve as both the high-Z sensitizer and the primary fluorophore [28–30], or as the secondary fluorophore pumped by the plastic matrix [31, 32]. Efficient energy transfer (both nonradiative and radiative) between each component (matrix → QDs, QDs → dye, QDs-matrix → dye) was readily demonstrated [11, 30]. However, the contribution of high-Z sensitization by QDs to scintillation LY is difficult to quantify and may even be underestimated. In conventional organic liquid scintillators, most X/γ-ray energy is considered to be deposited in the solvent due to its dominant volume fraction [33]. By contrast, recent Compton-Triple to Double Coincidence Ratio experiments on $CsPbBr_3$ QDs liquid scintillators indicated that when X/γ-rays interact with QDs liquid scintillators, QDs possess a higher interaction probability than the organic components [34], with the fraction of deposited energy dependent on QDs concentration—in agreement with X-ray based scintillation studies on the same QDs systems [10]. This behavior suggests that in QD-based composite scintillators, QDs play a crucial role in primary energy deposition and secondary electron showers. However, the detailed mechanisms governing energy deposition and conversion within these hybrid nanocomposites remain to be fully elucidated. This would provide a rational guide for maximizing energy transfer pathways for achieving highly efficient sensitized nano-scintillators.

The development of nanomaterials has provided numerous options for sensitized scintillators while also creating demand for highly performing organic emitting materials. Conjugated polymers have been proposed as materials for detecting radiation since the 1980s based on either their electrical or optical properties [35–38]. A particularly advantageous feature of π-conjugated polymers, especially for ultrafast scintillators, is their ability to exhibit emission spectra in the green-yellow region, spectrally decoupled from the typical radiation-induced absorption bands in plastic matrices (usually in the UV-blue region) [39], while maintaining emission rates significantly higher than those of conventional molecular emitters [40]. This behavior arises from the delocalization of the excitonic wavefunction over multiple conjugated monomeric units, which on the one hand leads to smaller energy gaps compared to isolated repeat units, resulting in a red-shift of the optical spectra, and on the other hand produces a much larger oscillator strength (analogous to the so-called *giant oscillator strength* in traditional semiconductors) [9]. As a consequence, these materials display ultrafast radiative decay rates (<2 ns) despite their lower emission energy, which would otherwise imply slower emission. As a result, conjugated polymers are known to be faster than organic molecules emitting in the same spectral region. This opens the way to high scintillation speeds and enhanced radiation stability, aligning with the emerging research trend toward ultrafast plastic-based calorimeters for high luminosity colliders. An additional advantage, which is no less important than the photophysical aspects, of conjugated polymers as emitters for nanocomposite scintillators lies in their versatility of use: they can function either as a luminescent filler dispersed within a higher-gap matrix (as is typical for conventional molecular emitters) or as the active scintillating matrix itself, where the entire material contributes to scintillation. This is particularly beneficial for scintillator coatings with high emitter density or for metascintillators combined with high-Z substrates (e.g., LYSO, BGO) [41]. In such configurations, the polymeric material not only eliminates the need for an external matrix that could generate unwanted background signals (for instance, the few-nanosecond blue luminescence of polyvinyl toluene or polystyrene) [11], but also partially mitigates LY losses by reducing competing energy-deposition channels. This application is further supported by the generally reduced π-π stacking of polymeric chains with respect to small organic moieties in the solid state, which commonly leads to strong intermolecular dimerization with lower emission yield, slower decay rates, and poorer spectral purity [42].

In this study, we report an efficient, fast sensitized scintillator based on NCs and the conjugated polymer poly(9,9-dioctylfluorene-alt-benzothiadiazole) (F8BT) featuring high photoluminescence (PL) quantum yield, Φ_{PL} (≈70% in toluene solution), fast decay time, largely Stokes shifted green-emission matching solid-state photodetectors, and ease of fabrication [43–45]. We also use F8BT-nanocrystal blends as model systems for clarifying the energy conversion mechanisms underlying high-Z and optical sensitization in hybrid nanoscintillators. As sketched in Figure 1a, we conducted a comparative study using two types of nanoscale sensitizers with distinct sensitization pathways. Specifically, HfO_2 NCs (hereafter indicated as NCs) were chosen as non-emissive high-Z sensitizers that generate secondary photoelectrons under X-ray excitation that subsequently excite F8BT moieties. By contrast, highly luminescent CdZnS/ZnS core/shell QDs (hereafter indicated as CZS QDs) provide dual high-Z and optical sensitization, delivering energy to F8BT via both secondary electrons and their intrinsic blue emission. In both systems, F8BT serves as the energy acceptor and matrix, obviating the need for additional host materials and enabling efficient energy collection and rapid photophysical dynamics. Radioluminescence (RL) measurements on composites with matched stopping power—validated by Geant4 Monte Carlo simulations—show that the CZS/F8BT system exhibits a scintillation efficiency more than twice that of HfO_2/F8BT and roughly 70 times higher than that of non-sensitized F8BT. Notably, consistent with previous reports [16, 46], the LY of HfO_2-sensitized F8BT decreases with increasing NCs loading, indicating that the sensitizers act as passive energy-dissipation centers for their own electron showers. In contrast, the LY of CZS/F8BT blends remains constant across all QD concentrations, even at the highest loadings, demonstrating that emissive CZS QDs effectively recycle secondary excitations and further

16163028, 0, Downloaded from https://advanced.onlinelibrary.wiley.com/doi/10.1002/adfm.74942 by Universita Milano Bicocca, Wiley Online Library on [07/04/2026]. See the Terms and Conditions (https://onlinelibrary.wiley.com/terms-and-conditions) on Wiley Online Library for rules of use; OA articles are governed by the applicable Creative Commons License

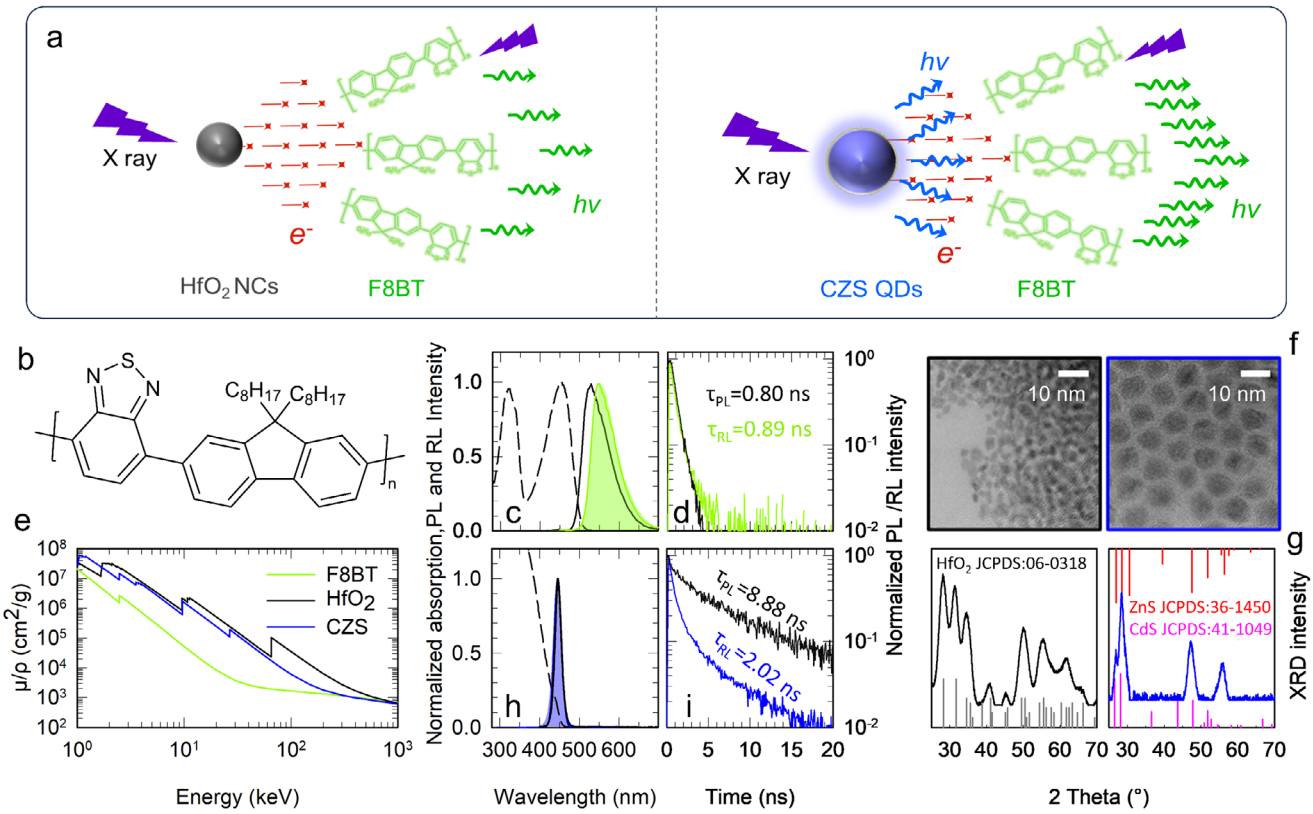

FIGURE 1 | Design concept and basic characterization of NCs/QDs and F8BT. (a) Sketch of the two sensitization pathways: high-Z sensitization in HfO_2/F8BT (top) and dual (high-Z and optical) sensitization in CZS/F8BT blends (bottom). (b) Molecular structure of F8BT. (c) Normalized absorption (dashed lines), PL spectra in solution (black solid lines) and films (green solid lines), and RL spectra in films (green shaded areas) of F8BT. (d) Normalized TRPL and TRRL of F8BT film (550 nm). (e) X-ray mass attenuation coefficients (μ/ρ) of F8BT, HfO_2, and CZS. (f) TEM images of HfO_2 NCs (left) and CZS QDs(right). (g) XRD patterns of HfO_2 NCs (top) and CZS NCs (bottom). Grey patterns refer to the corresponding references. (h) Normalized absorption (dashed lines), PL spectra in solution (black solid lines) and films (blue solid lines), and RL spectra in films (blue shaded areas) of CZS QDs. (i) Normalized TRPL and TRRL of CZS QDs film (445 nm).

underscoring the advantages of dual sensitization. Both hybrid scintillators also exhibit ultrafast decay times ≤ 2.6 ns. Finally, we confirm the feasibility of α-particle detection using nanocrystal-blended polymer films, highlighting the practical potential of these materials for radiation sensing. Collectively, these results establish a design framework for hybrid nanocrystal/polymer scintillators that combines high LY, rapid decay, and simple processing, with broad implications for next-generation high-performance scintillators.

2 | Results and Discussion

Figure 1a summarizes the design concept and fundamental characterization of the nanocrystals and polymer studied in this work. F8BT is a conjugated donor–acceptor copolymer comprising alternating 9,9-dioctylfluorene and benzothiadiazole units [45] (Figure 1b). Its strong π–π conjugation gives rise to a broad absorption band (a double peak) and a relatively large Stokes shift (≈70–90 nm, Figure 1c), minimizing self-absorption losses. It is noted that the photoluminescence (PL) spectrum of F8BT undergoes a slight red shift in the film state relative to solution, with the Φ_{PL} decreasing from ≈72% to ≈26%, while the PL lifetime shortens proportionally from 2.9 ns to 0.8 ns (Figure S1) as typically attributed to π-π stacking [43, 44, 47]. We anticipate that such efficiency loss is recovered by ≈90% upon blending with NCs that hinder interchain aggregation (vide infra) [48–50]. The RL and PL behavior of the film sample are consistent, with unchanged spectral shapes and positions, and lifetimes of ≈0.8 ns.

To quantitatively evaluate the two different sensitization mechanisms, careful selection of the energy donors is critical. Beyond maximizing X-ray absorption, the components must ensure efficient energy transfer (ET) and preserve fast photophysics, thereby enabling high scintillation efficiency and fast decay time. Figure 1e shows the X-ray mass attenuation coefficients of F8BT, HfO_2 NCs and CZS QDs, which highlight the superior X-ray stopping power of both types of NCs relative to F8BT and thus support their selection as high-Z sensitizers. Importantly, at 10 keV, the attenuation coefficients of HfO_2 and CZS are nearly identical, indicating comparable stopping power under our experimental conditions. This equivalence is a crucial prerequisite for the subsequent quantitative comparison of scintillation yield. CZS QDs were synthesized via hot-injection method [28, 51, 52], whereas HfO_2 NCs were obtained by the thermal decomposition of $Hf(CF_3COO)_4$ precursors [15, 16, 27]. Figure 1f displays the transmission electron microscopy (TEM) images of HfO_2 NCs and CZS QDs, showing average diameters of approximately 5 nm and 11.5 nm respectively, and clear lattice fringes indicative of high crystallinity. X-ray diffraction (XRD) patterns further confirm

16163028, 0, Downloaded from https://advanced.onlinelibrary.wiley.com/doi/10.1002/adfm.74942 by Universita Milano Biococa, Wiley Online Library on [07/04/2026]. See the Terms and Conditions (https://onlinelibrary.wiley.com/terms-and-conditions) on Wiley Online Library for rules of use; OA articles are governed by the applicable Creative Commons License

their phase purity, with HfO_2 NCs matching the monoclinic phase and CZS QDs showing a hexagonal structure. Figure S2 shows detailed (S)TEM characterization (panels (a), (d)) of the CdZnS QD cores and CdZnS/ZnS core/shell QDs. Crystalline phases of both systems are confirmed to be the hexagonal wurzite phase by HRTEM images and related FFTs (panels (b) and (c), (e) and (f)). Energy-dispersive X-ray (EDX) spectroscopy analysis on multiple sites show the co-presence of Cd, Zn and S on all QDs (panels (g), (h)). The chemical compositions (averaged) of the core-only and core/shell QDs are $Cd_{0.65}Zn_{0.35}S$ and $Cd_{0.19}Zn_{0.81}S$, respectively. All CZS-related analysis in this paper is based on this composition. Hereafter, all studies are conducted with core/shell QDs.

The optical properties of the selected QDs further support this design. CZS QDs exhibit intense blue emission (Φ_{PL}≈80%) centered at 445 nm under both optical and X-ray excitation (Figure 1h). This emission wavelength is mainly determined by the Cd:Zn ratio in the particle core [51], corresponding to Cd:Zn = 0.6:0.4, which is consistent with the EDX results. Benefiting from its thick shell and alloyed core-shell transition layer, this stable QDs exhibit only a slight decrease in Φ_{PL} and lifetime when fabricated into thin film (Figure S3a) [53]. The emission wavelength provides near-perfect spectral overlap with the F8BT absorption band, enabling highly efficient radiative and nonradiative ET. The average lifetimes of the PL and RL of CZS QDs 8.9 ns and 2 ns, respectively (Figure 1i). The RL decay kinetics shows the expected multi-excitonic profile, with an initial fast biexciton component (τ_{XX} = 0.9 ns) followed by the single exciton decay with lifetime comparable to the low-fluence PL to 8.9 ns [54–56]. This ascription is supported by the equivalence of the RL decay to the transient absorption kinetics as a function of the excitation fluence reported in Figure S3b, from which we quantify the biexciton yield $\Phi_{XX} = \frac{k_{XX}}{k_{XX}^{RAD}}$ =32% (see Supporting Information for details), consistent with the core/shell structure of the QDs [57].

Blended films were fabricated by drop casting mixed dispersions of F8BT with HfO_2 NCs or CZS QDs at sensitizer-to-F8BT mass ratios of 2:1, 5:1, 10:1, 20:1, and 50:1. Hereafter, we refer to each sample by the numerical value of this ratio—for example, the 50:1 composition is denoted as [NC] = 50 w/w. Across each series, the absolute F8BT quantity was kept constant, and only the content of sensitizers was varied. Pure F8BT and pure CZS QDs films were also fabricated as control samples. To assess sample quality, absorption spectra were recorded for all solutions and films (Figure S4). For HfO_2/F8BT, the solution spectra remained unchanged across all loadings, indicating negligible scattering. In the film state, absorption above ≈500 nm also showed minimal variation, suggesting limited impact on the emission-relevant region. The less systematic variations observed around the intrinsic absorption features (e.g., near ≈330 nm and ≈470 nm) are possibly attributed to film non-uniformity. In contrast, CZS/F8BT samples exhibit a slight increase in baseline at high loadings, more evident in the film state, which is attributed to some light scattering effects associated with the larger size and higher volume fraction of CZS QDs.

Consistent with the wide bandgap and optical inertness of HfO_2 NCs, the HfO_2/F8BT films exhibit only the F8BT green emission, with no change in the spectral shape as the HfO_2 NCs content increases (Figure 2a). Remarkably, the integrated PL intensity increases with the addition of the NCs corresponding to Φ_{PL} = 65% at the highest NCs content accompanied by the concomitant increase of the PL lifetime (Figure 2b). We attribute this to reduced interchain π–π stacking in the presence of HfO_2 NCs that act as physical spacers between F8BT moieties, in agreement with recent reports on polyfluorene/NCs blends [48–50]. Figure 2c shows this concerted PL and lifetime behavior, indicating that HfO_2 improves the photophysical environment of the polymer without introducing new nonradiative channels, enabling brighter PL at essentially unchanged spectral characteristics.

Under 360 nm excitation, CZS/F8BT films display a dual-band PL comprising the CZS QDs blue emission and the F8BT green band (Figure 2d). Increasing the QDs loading leads to an overall intensity rise in both bands (Figure 2f). In this blend, CZS QDs play two roles. Similar to HfO_2 NCs, they act as physical spacers hindering interchain aggregation. Independent support comes from Φ_{PL} and TRPL measured under acceptor-only excitation at 475 nm (Figure S5) that reaches 66% at the highest QDs content. At the same time, it serves as an emissive energy donor whose blue PL overlaps the F8BT absorption. Because CZS QDs and F8BT are in direct contact within the blend, their donor-acceptor separations lie within the resonant ET range (≈5.5 nm, see Methods), enabling efficient ET that funnels a fraction of the QDs excitation into the F8BT channel. Consistently, the lifetime of the QDs donors (Figure 2e, inset) in the blend is significantly shorter than that in pure QDs film, and this shortening accelerates as the acceptor content increases (relative to the donor content). This is a typical characteristic of resonant ET kinetics, yielding an energy transfer efficiency $\Phi_{ET} = 1\text{-}\tau_{DA}/\tau_D$ = 0.75—notice that the incomplete Φ_{ET} is fully consistent with the typical phase separation present in polymeric blends that is further enhanced at very high QDs loadings. In parallel, the F8BT decay at 550 nm progressively lengthens, mirroring the behavior observed in HfO_2/F8BT and attributable to the spacer-like action of QDs. We notice that despite the presence of the ET pathway, in the CZS/F8BT blend, the F8BT PL intensity remains comparable to that of the HfO_2 /F8BT system. This is because in the CZS/F8BT blend, the QDs and F8BT competitively absorb 360 nm excitation photons, and Φ_{ET} <1. Unlike the HfO_2/F8BT blends, high-loading CZS/F8BT films exhibit a slow tail in the F8BT PL decay (Figure 2e). Because ET preserves the acceptor's intrinsic lifetime, this long-lived component is assigned to emission-reabsorption of the blue QDs photons in the optically dense blends, resulting in a distinct decay tail that closely matches the lifetime of CZS QDs not directly involved in the ET process—also in agreement with Φ_{ET} being less than unity.

After establishing the photophysics under optical pumping, we turned to X-ray excitation to evaluate scintillation output and dynamics. For HfO_2/F8BT, the RL spectra display only the F8BT green band, and the RL intensity increases with the HfO_2 NCs content, gradually approaching saturation ≈25× the pure F8BT RL intensity at high loading (Figure 3a,b). The enhancement here is due to high-Z sensitization, with a net contribution of approximately 9.6× (after subtracting the portion directly excited by X-rays in F8BT and accounting for changes in Φ_{PL}). In contrast, CZS/F8BT exhibits dual-band RL with CZS blue and

16163028, 0, Downloaded from https://advanced.onlinelibrary.wiley.com/doi/10.1002/adfm.74942 by Universita Milano Bicocca, Wiley Online Library on [07/04/2026]. See the Terms and Conditions (https://onlinelibrary.wiley.com/terms-and-conditions) on Wiley Online Library for rules of use; OA articles are governed by the applicable Creative Commons License

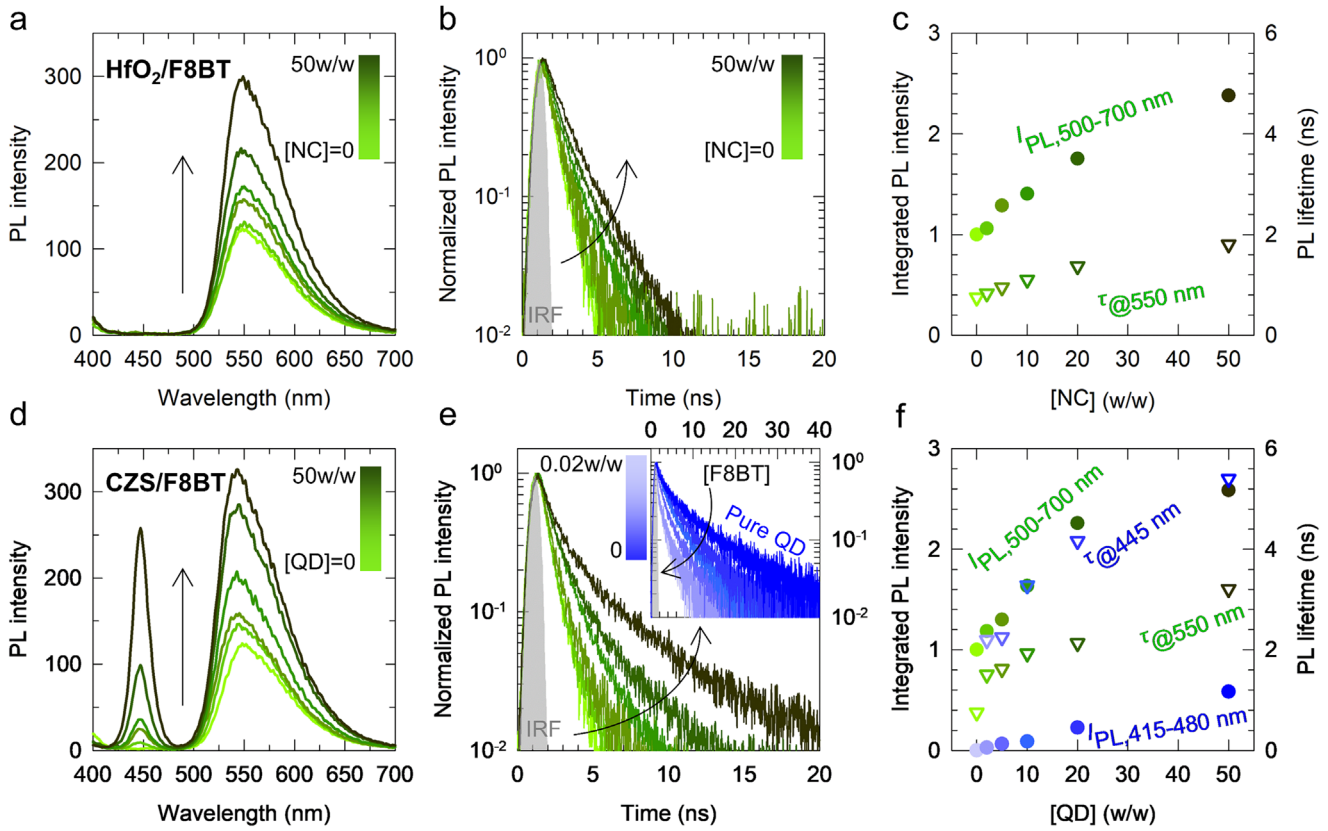

FIGURE 2 | Optical properties of NCs/F8BT blend films. (a) PL spectra of HfO_2/F8BT films at increasing [NC] as indicated by the arrow (from pure F8BT to [NC] = 50 w/w), excited at 360 nm. (b) Corresponding PL decay curves of HfO_2/F8BT blends at increasing [NC], monitored at 550 nm. (c) Integrated F8BT PL intensity (circle) (normalized to integral intensity of pure F8BT film) and PL lifetimes (triangle) at increasing [NC]. (d) PL spectra of CZS/F8BT films at increasing [QD] as indicated by the arrow (from pure F8BT to [QD] = 50 w/w), excited at 360 nm. (e) Corresponding PL decay curves of CZS/F8BT blends at increasing [QD], monitored at 550 nm (green, same color scheme as in 'd') and 445 nm (inset, blue color bar). All TRPL spectra were normalized to their maxima; excitation wavelength was 340 nm. (f) Integrated CZS (blue) and F8BT (green) PL intensity (circle) (normalized to the integrated intensity of pure F8BT film) and average PL lifetimes extracted from biexponential fitting of the curves in 'e' (triangle, see Supporting Information for details) at increasing [QD].

F8BT green emission contributions, both rising nearly linearly with QDs loading (Figure 3c,d). At the highest QD content, the F8BT RL reaches ≈60× that of the pure polymer, substantially exceeding the HfO_2 NCs case and indicating an additional optical sensitization pathway beyond pure high-Z effects. From an application perspective, the residual blue light emission from QDs also contributes to the overall scintillation output. When accounting for this blue light component, the total light output is 70 times that of pure F8BT. Figure S6 compares the ratio of the QDs and F8BT integrated emission intensity (I_{QD}/I_{F8BT}) in the PL and RL spectra of the CZS/F8BT sample vs [QD]. RL exhibits a smaller slope, which is attributed to the contribution of high-Z sensitization, which boosts the polymer emission relative to the QDs. To accurately evaluate the two contributions, we prepared CZS/PMMA reference films at the same mass ratios. The CZS@PMMA reference RL spectra (Figure S7) represent the donor output before energy transfer, from which the number of transferred photons can be obtained. By further considering the Φ_{PL} of F8BT (corrected for the spacing effect by the QDs), the optical sensitized photons can be estimated. Subsequently, the high-Z contribution is obtained by subtracting the directly excited F8BT portion and the optical sensitization portion from the total photons (see the Methods section). Figure 3e illustrates the contributions of F8BT direct excitation, high-Z sensitization, and optical sensitization to the scintillation efficiency under different loading conditions. These RL values include the contribution from the PLQY increase induced by the "spacing effect." Figure S8 presents the decoupled contributions normalized by PL intensity. At the highest loading, the ratio of high-Z: optical contribution is 8.3:14.9, confirming that both pathways play significant roles in enhancing RL.

To understand these distinct RL trends, we evaluated the X-ray energy deposition using GEANT4 simulation, using the material parameters (composition, density, and thickness) summarized in Table S1. As shown in Figure S9, with increasing NCs/QDs loading, the fraction of interacting X-ray photons (f_{Int}) rises linearly, while the mean deposited energy per interaction saturates due to increased film density and thickness. As a result, the total deposited energy fraction ($f_{E,dep}$) exhibits sublinear growth. Notably, HfO_2/F8BT exhibits higher deposited energy than CZS/F8BT at identical loadings, helping to explain the stronger high-Z sensitization observed in Figure S8. Beyond absorption differences, this may also reflect the influence of nanocrystal size on sensitization efficiency: the smaller HfO_2 NCs are more effective at releasing energy to the surrounding polymer

16163028, 0, Downloaded from https://advanced.onlinelibrary.wiley.com/doi/10.1002/adfm.74942 by Universita Milano Bicocca, Wiley Online Library on [07/04/2026]. See the Terms and Conditions (https://onlinelibrary.wiley.com/terms-and-conditions) on Wiley Online Library for rules of use; OA articles are governed by the applicable Creative Commons License

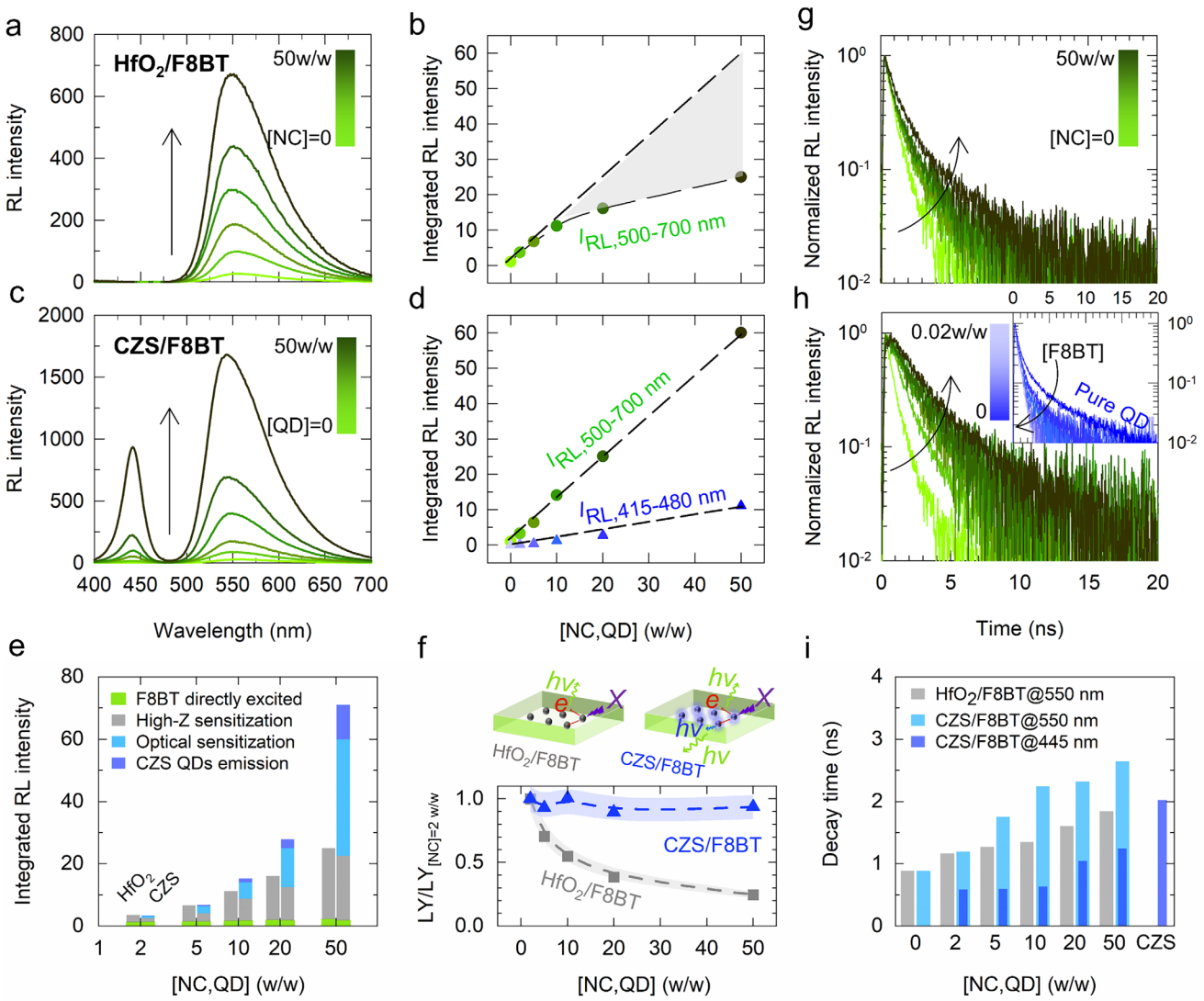

FIGURE 3 | Radioluminescence properties of NCs/F8BT blend films. (a) RL spectra of HfO_2/F8BT films at increasing [NC] as indicated by the arrow (from pure F8BT to [NC] = 50 w/w). (b) Integrated F8BT RL intensity at increasing [NC] (normalized to integral intensity of pure F8BT film), the grey shaded area highlights the efficiency loss with increasing [NC]. (c) RL spectra of CZS/F8BT films at increasing [QD] as indicated by the arrow (from pure F8BT to [QD] = 50 w/w). (d) Integrated CZS (blue) and F8BT (green) RL intensity at increasing [QD] (normalized to integral intensity of pure F8BT film). (e) Stacked bar chart of RL contributions at each NCs/QDs loading, showing the partition among direct F8BT excitation (green), high-Z sensitization (gray), optical sensitization (light blue), and CZS QDs emission (dark blue). (f) Light yield of HfO_2/F8BT and CZS/F8BT films, normalized to LY at NCs/F8BT = 2 w/w. The schematic highlights distinct energy-flow pathways at high nano-sensitizer loadings, where secondary electrons are increasingly trapped by neighboring NCs and dissipated non-radiatively in HfO_2 but partially recovered through radiative emission and donor-to-acceptor optical sensitization in CZS films. (g) TRRL of F8BT in HfO_2/F8BT blends at increasing [NC], monitored at 550 nm. (h) TRRL of CZS/F8BT blends at increasing [QD], monitored at 550 nm (green) and 445 nm (blue insert). All TRRL spectra were normalized to their maxima. (i) Intensity-weighted average lifetimes extracted from f,g (double-exponential fitting), comparing the two series. Pure F8BT (green) and pure CZS (blue) films are shown as controls.

matrix during both primary X-ray interactions and secondary electron cascades.

By combining RL measurements (Figure S10) with GEANT4-simulated deposited energy, the LY was obtained (see Methods for details). Figure 3f shows the different normalized LY trends of the two systems: HfO_2/F8BT shows a gradual decrease in LY with increasing NCs loading, whereas CZS/F8BT maintains an almost constant LY across all compositions. This contrast arises from secondary-electron capturing at high NCs fractions. As the NCs loading increases, the secondary electrons produced by X-ray absorption are increasingly intercepted by neighboring NCs before reaching the polymer matrix (Figure 3f). Within HfO_2, a portion of the deposited energy is dissipated non-radiatively. This is primarily attributed to the wide bandgap of HfO_2 and the lack of radiative recombination centers, which cause electronic excitations from secondary electrons to rapidly thermalize and relax via phonon-assisted processes (shaded area in Figure 3b). In CZS QDs, however, a substantial portion of the trapped energy is re-emitted radiatively or recycled through donor-acceptor optical sensitization. This behavior mirrors the self-sensitization mechanism of perovskite QDs we previously identified in dense

16163028, 0, Downloaded from https://advanced.onlinelibrary.wiley.com/doi/10.1002/adfm.74942 by Universita Milano Bicocca, Wiley Online Library on [07/04/2026]. See the Terms and Conditions (https://onlinelibrary.wiley.com/terms-and-conditions) on Wiley Online Library for rules of use; OA articles are governed by the applicable Creative Commons License

mesoporous nanosphere structures [26]. Therefore, CZS QDs exhibits intrinsically higher energy-conversion efficiency than HfO_2 NCs under identical loading conditions. The LY values should be interpreted with caution, as they are estimates derived from RL measurements (referenced to BGO with LY ≈9000 ph MeV^{-1}) corrected using GEANT4-simulated deposited energies rather than direct measurement [58]. Although this introduces systematic bias, the relative trends remain robust. Under the highest NC loading (minimum error), the X-ray LY is conservatively estimated at ≈9210 ph MeV^{-1} for HfO_2/F8BT and −2950 ph MeV^{-1} for CZS/F8BT. Here we focus on thin-film composites for low-energy X-ray detection. For higher-energy γ-ray detection, high-Z loading is a general strategy to improve γ-ray detection efficiency. Our results further suggest a broader implication for γ-ray scintillators: while heavy-element loading is often accompanied by a reduction in LY at high loading, incorporating luminescent High-Z nanocrystals that enable photon recycling (dual sensitization) offers a route to mitigate this long-standing trade-off. This strategy is thus promising for designing composite scintillators that combine improved γ-ray detection efficiency with higher LY.

Time-resolved RL further clarifies the dynamics. Overall, the RL kinetics (Figure 3g,h) resemble the PL behavior. The lifetime in the F8BT (550 nm) channel increases with increasing NCs content in both cases, further confirming the spacing effect suppressing non-radiative losses on the acceptor side. For HfO_2/F8BT, unlike the single-exponential PL decay, the RL kinetics show a double-exponential decay with a weak, slow tail. In principle, high-Z sensitization does not modify the acceptor's intrinsic radiative rate. The slow component may be associated with defect-state emission or irradiation-induced shallow traps introduced by HfO_2 NCs. Overall, the decay remains dominated by the intrinsic fast F8BT emission, the slow fraction is minor, and the decay times remain ≤ 1.8 ns. For CZS/F8BT, the donor channel at 445 nm decays faster under RL than under optical excitation, consistent with the multi-excitonic character of scintillation in quantum confined particles [10, 56, 59]. Meanwhile, as the CZS QDs loading increases, the rise time of F8BT at 550 nm increases, reflecting higher optical sensitization due to radiation energy mainly depositing within the CZS QDs. In TRPL experiments, the effect is hidden by direct optical excitation of F8BT. We fitted all RL decay traces with a bi-exponential function and report the effective lifetimes, τ_{EFF} (calculated as the weighted harmonic average of the decay components, see Methods) in Figure 3i. The HfO_2/F8BT series retains $\tau_{EFF} \leq 1.8$ ns acceptor-dominated kinetics. In the CZS/F8BT, donor lifetimes are typically ≤ 1.2 ns while acceptor lifetimes remain ≤ 2.6 ns, resulting in acceptor-dominated $\tau_{EFF} \leq 2.6$ ns decay. The timing properties of this sensitized scintillator are significantly better than those of commercial green scintillators such as EJ-260 (9.2 ns) [60] and BC428 (12.5 ns) [61]. These dual-sensitized scintillators deliver comparable or superior timing together with markedly higher scintillation efficiency, highlighting a practical pathway to fast, efficient scintillators via dual sensitization.

Finally, having established efficient RL output and fast kinetics under X-ray excitation, we evaluate the feasibility of α-particle detection with the blend films. Unlike X-/γ-rays, which deposit energy predominantly via the photoelectric effect/Compton scattering, α particles are highly ionizing heavy charged particles with short ranges and strongly localized energy loss that peaks near the end of the track (Bragg peak) [62]. These characteristics give thin-film scintillators distinct advantages: their thickness can completely block α particles while allowing energy readout, combined with solution processability, short optical path scattering benefits, and the simplicity of direct coupling to photodetectors. Monte Carlo simulations for 5.5 MeV α particles from ^{241}Am quantify transport and stopping in the three films (highest loading). Tracks are quasi-linear with modest terminal scattering (Figure 4a). Due to differences in composition and density, the projected ranges are about 35 µm (F8BT), 20 µm (HfO_2/F8BT), and 27.5 µm (CZS/F8BT). The corresponding Bragg curve exhibits a clear Bragg peak and shows the relationship between energy loss and depth. The simulation results provide a basis for the experiment.

In the experiment, films approximately 40 µm thick were drop-cast onto a transparent quartz substrate. This thickness is sufficient to completely block 5.5 MeV α particles. The experimental test setup consists of a silicon photomultiplier (SiPM) testing system in a vacuum chamber. By adjusting the chamber pressure (keep the same distance of 5 cm), the effective α particle energy reaching the sample can be tuned [63]. The samples were coupled to the SiPM using optical grease to read the optical signal, with waveform signals recorded and stored by an oscilloscope. The sample's surface opposite the SiPM was exposed to the α particles. As shown in Figure 4c, at low pressures the CZS/F8BT film exhibits a clearly resolved full-energy peak, whereas pure F8BT and HfO_2/F8BT exhibit signals (confirm from Figure S11) but no distinguishable alpha peaks, consistent with the substantially higher LY of the dual-sensitized CZS/F8BT system. Increasing the pressure reduces the incident α energy and causes the peak of the energy spectrum to shift to lower channel in CZS/F8BT (Figure 4d), confirming the fundamental energy resolution capability of this sample.

Due to the large dE/dx of α particles, localized high excitation and ionization densities typically lead to a reduction in scintillation efficiency, known as ionization quenching [64, 65]. The α particles' LY of organic scintillators is typically lower than that of inorganic scintillators, as their quenching factor (α/β ratio, the LY for α particles per MeV and that for β particles per MeV) being 2–4 times smaller [66]. Therefore, introducing inorganic QDs into organic polymers could suppress this quenching effect. Regarding the dynamics, in organic scintillators, the ionization quenching (singlet excited state) induced by α particles typically increases the proportion of the delayed component (triplet-triplet annihilation, TTA) [13, 33]. The incorporation of inorganic QDs plays a dual role in enhancing the α decay time of organic scintillators. On one hand, it reduces the excitation density within the organic matrix, suppressing the TTA process. On the other hand, a higher initial excitation density promotes multiple exciton/Auger recombination pathways within the QDs, further accelerating the decay time. Therefore, the α pulse decay time is expected to be nanoseconds or even faster. For reference, commercial α-scintillator ZnS:Ag powders typically exhibit a primary decay time of ≈180 ns, accompanied by µs-scale afterglow caused by defects [67–70]. Although the fast decay was not directly measured due to the time resolution limitations of the SiPM, we propose a promising solution for high-speed α-counting and spectroscopy.

16163028, 0, Downloaded from https://advanced.onlinelibrary.wiley.com/doi/10.1002/adfm.74942 by Universita Milano Biococa, Wiley Online Library on [07/04/2026]. See the Terms and Conditions (https://onlinelibrary.wiley.com/terms-and-conditions) on Wiley Online Library for rules of use; OA articles are governed by the applicable Creative Commons License

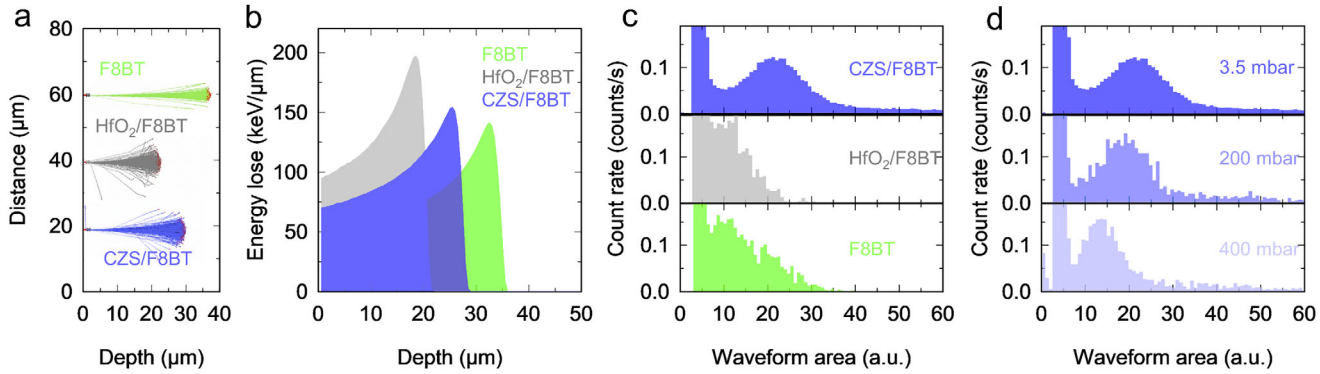

FIGURE 4 | Proof of concept of α particle detection using NCs/F8BT blend films. Monte Carlo simulation of 5.5 MeV α particle interactions with samples: (a) Projected incident trajectories of α particles in three thin films; (b) Bragg curves for α particles in three thin films (energy loss vs incident depth). (c) α particle energy spectra of the three films at same low pressure. (d) α particle energy spectra of the CZS/F8BT film at different pressures.

In conclusion, we have designed hybrid scintillators by blending a conjugated polymer with either non-emissive (HfO_2) NCs or emissive (CZS) QDs, enabling a quantitative dissection of high-Z sensitization and optical sensitization mechanisms. We show that dual sensitization dramatically enhances scintillation performance, yielding up to a 70-fold increase in X-ray light output relative to pure F8BT. Benefiting from F8BT intrinsically fast lifetime, the multiexciton-assisted dynamics of CZS QDs, and efficient donor–acceptor FRET, the blends maintain $\leq$ 2.6 ns decay kinetics. α-particle spectroscopy further confirms the capability of these films for heavy charged-particle detection. This work establishes a design blueprint for NCs-sensitized conjugated-polymer scintillators, overcoming the low stopping power of pure polymers and the self-absorption losses of QDs. Importantly, it highlights conjugated polymers as ideal energy acceptors, leveraging their high emission efficiency, ultrafast timing, solution processability, and the elimination of additional matrices. These results offer a versatile platform for developing efficient, fast, and easily processable scintillators for applications ranging from X-ray imaging to charged-particle detection.

Acknowledgements

This work was funded by Horizon Europe EIC Pathfinder program through project 101098649 – UNICORN, by the European Union - Next Generation EU, Mission 4 Component 1 CUP H53D23004670006, and through the Italian Ministry of University and Research under PNRR—M4C2-I1.3 Project PE_00000019 "HEAL ITALIA."

Open access publishing facilitated by Universita degli Studi di Milano-Bicocca, as part of the Wiley - CRUI-CARE agreement.

Conflicts of Interest

The authors declare no conflicts of interest.

Data Availability Statement

The data that support the findings of this study are available from the corresponding author upon reasonable request.

References

1. C. Dujardin, E. Auffray, E. Bourret-Courchesne, et al., "Needs, Trends, and Advances in Inorganic Scintillators," *IEEE Transactions on Nuclear Science* 65 (2018): 1977–1997, https://doi.org/10.1109/TNS.2018.2840160.

2. C. Dujardin, A. Bessière, A. Bulin, F. Chaput, and B. Mahler, "Inorganic Nanoscintillators: Current Trends and Future Perspectives," *Advanced Optical Materials* 13 (2025): 2402739, https://doi.org/10.1002/adom.202402739.

3. A. Anand, M. L. Zaffalon, A. Erroi, F. Cova, F. Carulli, and S. Brovelli, "Advances in Perovskite Nanocrystals and Nanocomposites for Scintillation Applications," *ACS Energy Letters* 9 (2024): 1261–1287, https://doi.org/10.1021/acsenergylett.3c02763.

4. Q. Chen, J. Wu, X. Ou, et al., "All-Inorganic Perovskite Nanocrystal Scintillators," *Nature* 561 (2018): 88–93, https://doi.org/10.1038/s41586-018-0451-1.

5. F. Cova, A. Erroi, M. L. Zaffalon, et al., "Scintillation Properties of $CsPbBr_3$ Nanocrystals Prepared by Ligand-Assisted Reprecipitation and Dual Effect of Polyacrylate Encapsulation toward Scalable Ultrafast Radiation Detectors," *Nano Letters* 24 (2024): 905–913, https://doi.org/10.1021/acs.nanolett.3c04083.

6. A. Erroi, S. Mecca, M. L. Zaffalon, et al., "Ultrafast and Radiation-Hard Lead Halide Perovskite Nanocomposite Scintillators," *ACS Energy Letters* 8 (2023): 3883–3894, https://doi.org/10.1021/acsenergylett.3c01396.

7. S. Mecca, F. Pallini, V. Pinchetti, et al., "Multigram-Scale Synthesis of Luminescent Cesium Lead Halide Perovskite Nanobricks for Plastic Scintillators," *ACS Applied Nano Materials* 6 (2023): 9436–9443, https://doi.org/10.1021/acsanm.3c01146.

8. A. Erroi, F. Carulli, F. Cova, et al., "Ultrafast Nanocomposite Scintillators Based on Cd-Enhanced $CsPbCl_3$ Nanocrystals in Polymer Matrix," *ACS Energy Letters* 9 (2024): 2333–2342, https://doi.org/10.1021/acsenergylett.4c00778.

9. M. L. Zaffalon, A. Fratelli, Z. Li, et al., "Ultrafast Superradiant Scintillation from Isolated Weakly Confined Perovskite Nanocrystals," *Advanced Materials* 37 (2025): 2500846, https://doi.org/10.1002/adma.202500846.

10. A. Fratelli, M. L. Zaffalon, E. Mazzola, et al., "Size-Dependent Multiexciton Dynamics Governs Scintillation from Perovskite Quantum Dots," *Advanced Materials* 37 (2025): 2413182, https://doi.org/10.1002/adma.202413182.

11. F. Carulli, A. Erroi, F. Bruni, et al., "Surface Modified $CsPbBr_3$ Nanocrystals Enable Free Radical Thermal Polymerization of Efficient Ultrafast Polystyrenic Nanocomposite Scintillators," *ACS Energy Letters* 10 (2025): 12–21, https://doi.org/10.1021/acsenergylett.4c02711.

16163028, 0, Downloaded from https://advanced.onlinelibrary.wiley.com/doi/10.1002/adfm.74942 by Universita Milano Bicocca, Wiley Online Library on [07/04/2026]. See the Terms and Conditions (https://onlinelibrary.wiley.com/terms-and-conditions) on Wiley Online Library for rules of use; OA articles are governed by the applicable Creative Commons License

12. M. L. Zaffalon, F. Cova, M. Liu, et al., "Extreme γ-ray Radiation Hardness and High Scintillation Yield in Perovskite Nanocrystals," *Nature Photonics* 16 (2022): 860–868, https://doi.org/10.1038/s41566-022-01103-x.

13. T. J. Hajagos, C. Liu, N. J. Cherepy, and Q. Pei, "High-Z Sensitized Plastic Scintillators: A Review," *Advanced Materials* 30 (2018): 1706956, https://doi.org/10.1002/adma.201706956.

14. W. Cai, Q. Chen, N. Cherepy, et al., "Synthesis of Bulk-Size Transparent Gadolinium Oxide–Polymer Nanocomposites for Gamma Ray Spectroscopy," *Journal of Materials Chemistry C* 1 (2013): 1970–1976, https://doi.org/10.1039/c2tc00245k.

15. C. Liu, T. J. Hajagos, D. Kishpaugh, et al., "Facile Single-Precursor Synthesis and Surface Modification of Hafnium Oxide Nanoparticles for Nanocomposite γ-Ray Scintillators," *Advanced Functional Materials* 25 (2015): 4607–4616, https://doi.org/10.1002/adfm.201501439.

16. H. Zhao, H. Yu, C. Redding, et al., "Scintillation Liquids Loaded with Hafnium Oxide Nanoparticles for Spectral Resolution of γ Rays," *ACS Applied Nano Materials* 4 (2021): 1220–1227, https://doi.org/10.1021/acsanm.0c02845.

17. Y. Jin, D. Kishpaugh, C. Liu, et al., "Partial Ligand Exchange as a Critical Approach to the Synthesis of Transparent Ytterbium Fluoride–Polymer Nanocomposite Monoliths for Gamma Ray Scintillation," *Journal of Materials Chemistry C* 4 (2016): 3654–3660, https://doi.org/10.1039/C6TC00447D.

18. M. Orfano, F. Pagano, I. Mattei, et al., "Fast Emitting Nanocomposites for High-Resolution ToF-PET Imaging Based on Multicomponent Scintillators," *Advanced Materials Technologies* 9 (2024): 2302075, https://doi.org/10.1002/admt.202302075.

19. M. Sala, M. Orfano, V. Secchi, et al., "Highly Luminous Scintillating Nanocomposites Enable Ultrafast Time Coincidence Resolution for γ-Rays Detection with Heterostructured Multilayer Scintillators," *Advanced Functional Materials* 35 (2025): 2421434, https://doi.org/10.1002/adfm.202421434.

20. A. Anand, M. L. Zaffalon, F. Cova, et al., "Optical and Scintillation Properties of Record-Efficiency CdTe Nanoplatelets toward Radiation Detection Applications," *Nano Letters* 22 (2022): 8900–8907, https://doi.org/10.1021/acs.nanolett.2c02975.

21. B. Guzelturk, B. T. Diroll, J. P. Cassidy, et al., "Bright and Durable Scintillation from Colloidal Quantum Shells," *Nature Communications* 15 (2024): 4274, https://doi.org/10.1038/s41467-024-48351-9.

22. X. Li, X. Hu, C. Li, et al., "Are Inorganic Lead Halide Perovskite Nanocrystals Promising Scintillators?," *ACS Energy Letters* 8 (2023): 2996–3004, https://doi.org/10.1021/acsenergylett.3c00920.

23. Z. Yang, J. Yao, L. Xu, W. Fan, and J. Song, "Designer Bright and Fast $CsPbBr_3$ Perovskite Nanocrystal Scintillators for High-Speed X-ray Imaging," *Nature Communications* 15 (2024): 8870, https://doi.org/10.1038/s41467-024-53263-9.

24. Z. Mi, H. Bian, C. Yang, Y. Dou, A. A. Bettiol, and X. Liu, "Real-Time Single-Proton Counting with Transmissive Perovskite Nanocrystal Scintillators," *Nature Materials* 23 (2024): 803–809, https://doi.org/10.1038/s41563-023-01782-z.

25. F. Carulli, F. Cova, L. Gironi, F. Meinardi, A. Vedda, and S. Brovelli, "Stokes Shift Engineered Mn:CdZnS/ZnS Nanocrystals as Reabsorption-Free Nanoscintillators in High Loading Polymer Composites," *Advanced Optical Materials* 10 (2022): 2200419, https://doi.org/10.1002/adom.202200419.

26. X. Zhou, M. L. Zaffalon, E. Mazzola, et al., "Harnessing Self-Sensitized Scintillation by Supramolecular Engineering of $CsPbBr_3$ Nanocrystals in Dense Mesoporous Template Nanospheres," *Advanced Materials* 38 (2026): 13469, https://doi.org/10.1002/adma.202513469.

27. F. Bruni, S. Chakraborty, A. Fratelli, et al., "Synergistic Compatibilization of $CsPbBr_3$ Perovskites and HfO_2 Nanocrystals for Hybrid Sensitized Nanoscintillators," *Advanced Functional Materials* (2025): e20228, https://doi.org/10.1002/adfm.202520228.

28. C. Liu, Z. Li, T. J. Hajagos, D. Kishpaugh, D. Y. Chen, and Q. Pei, "Transparent Ultra-High-Loading Quantum Dot/Polymer Nanocomposite Monolith for Gamma Scintillation," *ACS Nano* 11 (2017): 6422–6430, https://doi.org/10.1021/acsnano.7b02923.

29. H. Yu, T. Chen, Z. Han, J. Fan, and Q. Pei, "Liquid Scintillators Loaded with up to 40 Weight Percent Cesium Lead Bromide Quantum Dots for Gamma Scintillation," *ACS Applied Nano Materials* 5 (2022): 14572–14581, https://doi.org/10.1021/acsanm.2c02930.

30. M. Gandini, I. Villa, M. Beretta, et al., "Efficient, Fast and Reabsorption-Free Perovskite Nanocrystal-Based Sensitized Plastic Scintillators," *Nature Nanotechnology* 15 (2020): 462–468, https://doi.org/10.1038/s41565-020-0683-8.

31. S. Cho, S. Kim, J. Kim, et al., "Hybridisation of Perovskite Nanocrystals with Organic Molecules for Highly Efficient Liquid Scintillators," *Light: Science & Applications* 9 (2020): 156, https://doi.org/10.1038/s41377-020-00391-8.

32. M. Liu, L. Huang, D. Yuan, et al., "Perovskite Nanocrystals and Dyes for High-Efficiency Liquid Scintillator Counters To Detect Radiation," *ACS Applied Nano Materials* 6 (2023): 370–378, https://doi.org/10.1021/acsanm.2c04510.

33. M. Koshimizu, "Fundamental Processes and Recent Development of Organic Scintillators," *Journal of Luminescence* 278 (2025): 121008, https://doi.org/10.1016/j.jlumin.2024.121008.

34. M. Baravaglio, B. Sabot, F. Maddalena, et al., "Energy Deposition in Liquid Scintillators Composed of $CsPbBr_3$ Colloidal Nanocrystal Dispersions," *Nanoscale* 16 (2024): 17176–17186, https://doi.org/10.1039/D4NR02401J.

35. K. Yoshino, S. Hayashi, G. Ishii, and Y. Inuishi, "Electrical Transport in Electron Beam Irradiated Polyacetylene," *Solid State Communications* 46 (1983): 405–408, https://doi.org/10.1016/0038-1098(83)90458-1.

36. Q. Chen, T. Hajagos, and Q. Pei, "Conjugated Polymers for Radiation Detection," *Annual Reports Section "C" (Physical Chemistry)* 107 (2011): 298–318, https://doi.org/10.1039/c1pc90011k.

37. E. A. B. Silva, J. F. Borin, P. Nicolucci, C. F. O. Graeff, T. G. Netto, and R. F. Bianchi, "Low Dose Ionizing Radiation Detection Using Conjugated Polymers," *Applied Physics Letters* 86 (2005): 131902, https://doi.org/10.1063/1.1891300.

38. I. H. Campbell and B. K. Crone, "Quantum-Dot/Organic Semiconductor Composites for Radiation Detection," *Advanced Materials* 18 (2006): 77–79, https://doi.org/10.1002/adma.200501434.

39. P. M. Beaujuge and J. R. Reynolds, "Color Control in π-Conjugated Organic Polymers for Use in Electrochromic Devices," *Chemical Reviews* 110 (2010): 268–320, https://doi.org/10.1021/cr900129a.

40. W. Barford, "Exciton Dynamics in Conjugated Polymer Systems," *Frontiers in Physics* 10 (2022): 2022, https://doi.org/10.3389/fphy.2022.1004042.

41. G. Konstantinou, P. Lecoq, J. M. Benlloch, and A. J. Gonzalez, "Metascintillators for Ultrafast Gamma Detectors: A Review of Current State and Future Perspectives," *IEEE Transactions on Radiation and Plasma Medical Sciences* 6 (2022): 5–15, https://doi.org/10.1109/TRPMS.2021.3069624.

42. D. Barman, K. Narang, R. Parui, et al., "Review on Recent Trends and Prospects in π-Conjugated Luminescent Aggregates for Biomedical Applications," *Aggregate* 3 (2022): 172.

43. M. Mamada, R. Komatsu, and C. Adachi, "F8BT Oligomers for Organic Solid-State Lasers," *ACS Applied Materials & Interfaces* 12 (2020): 28383–28391, https://doi.org/10.1021/acsami.0c05449.

44. H. Zhang, D. Lei, B. Liu, Y. Guo, and D. Lu, "Effect of Solvation and Concentration on F8BT Chain Solution Behavior and Film Condensed Structure," *Polymer* 276 (2023): 125951, https://doi.org/10.1016/j.polymer.2023.125951.

16163028, 0, Downloaded from https://advanced.onlinelibrary.wiley.com/doi/10.1002/adfm.74942 by Universita Milano Bicocca, Wiley Online Library on [07/04/2026]. See the Terms and Conditions (https://onlinelibrary.wiley.com/terms-and-conditions) on Wiley Online Library for rules of use; OA articles are governed by the applicable Creative Commons License

45. J. Chappell, D. G. Lidzey, P. C. Jukes, et al., "Correlating Structure with Fluorescence Emission in Phase-Separated Conjugated-Polymer Blends," *Nature Materials* 2 (2003): 616–621, https://doi.org/10.1038/nmat959.

46. H. Yu, I. Winardi, Z. Han, D. Prout, A. Chatziioannou, and Q. Pei, "Fast Spectroscopic Gamma Scintillation Using Hafnium Oxide Nanoparticles–Plastic Nanocomposites," *Chemistry of Materials* 36 (2024): 533–540, https://doi.org/10.1021/acs.chemmater.3c02631.

47. C. L. Donley, J. Zaumseil, J. W. Andreasen, et al., "Effects of Packing Structure on the Optoelectronic and Charge Transport Properties in Poly(9,9-di-n-octylfluorene-alt-benzothiadiazole)," *Journal of the American Chemical Society* 127 (2005): 12890–12899, https://doi.org/10.1021/ja051891j.

48. J. Liu, J. Qiao, K. Zhou, et al., "An Aggregation-Suppressed Polymer Blending Strategy Enables High-Performance Organic and Quantum Dot Hybrid Solar Cells," *Small* 18 (2022): 2201387, https://doi.org/10.1002/smll.202201387.

49. A. Perevedentsev, N. Chander, J. Kim, and D. D. C. Bradley, "Spectroscopic Properties of Poly(9,9-dioctylfluorene) Thin Films Possessing Varied Fractions of β-Phase Chain Segments: Enhanced Photoluminescence Efficiency via Conformation Structuring," *Journal of Polymer Science Part B: Polymer Physics* 54 (2016): 1995–2006, https://doi.org/10.1002/polb.24106.

50. E. Dovgolevsky, S. Kirmayer, E. Lakin, Y. Yang, C. J. Brinker, and G. L. Frey, "Self-Assembled Conjugated Polymer–Surfactant–Silica Mesostructures and Their Integration into Light-Emitting Diodes," *Journal of Materials Chemistry* 18 (2008): 423–436, https://doi.org/10.1039/B713170D.

51. W. K. Bae, M. K. Nam, K. Char, and S. Lee, "Gram-Scale One-Pot Synthesis of Highly Luminescent Blue Emitting $Cd_{1-x}Zn_xS$/ZnS Nanocrystals," *Chemistry of Materials* 20 (2008): 5307–5313, https://doi.org/10.1021/cm801201x.

52. O. Wang, L. Wang, Z. Li, et al., "High-Efficiency, Deep Blue ZnCdS/$Cd_xZn_{1-x}S$/ZnS Quantum-Dot-Light-Emitting Devices with an EQE Exceeding 18%," *Nanoscale* 10 (2018): 5650–5657, https://doi.org/10.1039/C7NR09175C.

53. B. N. Pal, Y. Ghosh, S. Brovelli, et al., "'Giant' CdSe/CdS Core/Shell Nanocrystal Quantum Dots as Efficient Electroluminescent Materials: Strong Influence of Shell Thickness on Light-Emitting Diode Performance," *Nano Letters* 12 (2012): 331–336, https://doi.org/10.1021/nl203620f.

54. L. A. Padilha, W. K. Bae, V. I. Klimov, J. M. Pietryga, and R. D. Schaller, "Response of Semiconductor Nanocrystals to Extremely Energetic Excitation," *Nano Letters* 13 (2013): 925–932, https://doi.org/10.1021/nl400141w.

55. R. M. Turtos, S. Gundacker, S. Omelkov, et al., "On the Use of CdSe Scintillating Nanoplatelets as Time Taggers for High-Energy Gamma Detection," *npj 2D Materials and Applications* 3 (2019): 37, https://doi.org/10.1038/s41699-019-0120-8.

56. R. Turtos, S. Gundacker, A. Polovitsyn, et al., "Ultrafast Emission from Colloidal Nanocrystals under Pulsed X-ray Excitation," *Journal of Instrumentation* 11 (2016): P10015, https://doi.org/10.1088/1748-0221/11/10/P10015.

57. F. García-Santamaría, S. Brovelli, R. Viswanatha, et al., "Breakdown of Volume Scaling in Auger Recombination in CdSe/CdS Heteronanocrystals: The Role of the Core−Shell Interface," *Nano Letters* 11 (2011): 687–693, https://doi.org/10.1021/nl103801e.

58. M. L. Zaffalon, L. Gironi, M. Nikl, and S. Brovelli, "From Optoelectronics to Radiation Detection: Light Yield Challenges in Perovskite Scintillators," *ACS Energy Letters* 11 (2026): 31–42, https://doi.org/10.1021/acsenergylett.5c03188.

59. K. Lee, J. Lee, H. Kang, et al., "Highly Fluorescence-Stable Blue CdZnS/ZnS Quantum Dots against Degradable Environmental Conditions," *Journal of Alloys and Compounds* 610 (2014): 511–516, https://doi.org/10.1016/j.jallcom.2014.05.052.

60. Eljen Technology, *EJ-260 and EJ-262 Plastic Scintillators*, https://eljentechnology.com/products/plastic-scintillators/ej-260-ej-262.

61. Luxium Solutions, *BC-428 Green-Emitting Plastic Scintillator*, https://luxiumsolutions.com/radiation-detection-scintillators/plastic-scintillators/green-emitting-bc-428.

62. S. Yamamoto, Y. Hirano, K. Kamada, and A. Yoshikawa, "Development of an Ultrahigh-Resolution Radiation Real-Time Imaging System to Observe Trajectory of Alpha Particles in a Scintillator," *Radiation Measurements* 134 (2020): 106368, https://doi.org/10.1016/j.radmeas.2020.106368.

63. L. Gironi, S. Dell'Oro, C. Gotti, et al., "A Custom Experimental Setup for Scintillator Characterization: Application to a Ce-Doped GAGG Crystal," *The European Physical Journal Plus* 140 (2025): 415, https://doi.org/10.1140/epjp/s13360-025-06350-9.

64. J. B. Birks, "Scintillations from Organic Crystals: Specific Fluorescence and Relative Response to Different Radiations," *Proceedings of the Physical Society Section A* 64 (1951): 874–877, https://doi.org/10.1088/0370-1298/64/10/303.

65. T. A. Laplace, B. L. Goldblum, J. A. Brown, et al., "Modeling Ionization Quenching in Organic Scintillators," *Materials Advances* 3 (2022): 5871–5881, https://doi.org/10.1039/D2MA00388K.

66. W. Wolszczak and P. Dorenbos, "Nonproportional Response of Scintillators to Alpha Particle Excitation," *IEEE Transactions on Nuclear Science* 64 (2017): 1580–1591, https://doi.org/10.1109/TNS.2017.2699327.

67. G. J. Sykora, E. M. Schooneveld, and N. J. Rhodes, "ZnO:Zn/^{6}LiF Scintillator—A Low Afterglow Alternative to ZnS:Ag/6LiF for Thermal Neutron Detection," *Nuclear Instruments and Methods in Physics Research Section A: Accelerators, Spectrometers, Detectors and Associated Equipment* 883 (2018): 75–82, https://doi.org/10.1016/j.nima.2017.11.052.

68. S. E. Mann, E. M. Schooneveld, N. J. Rhodes, D. Liu, and G. J. Sykora, "Timing Properties of Radioluminescence in Nanoparticle ZnS:Ag Scintillators," *Optical Materials: X* 17 (2023): 100226, https://doi.org/10.1016/j.omx.2022.100226.

69. Q. Wang, C. Wang, H. Shi, et al., "Exciton-Harvesting Enabled Efficient Charged Particle Detection in Zero-Dimensional Halides," *Light: Science & Applications* 13 (2024): 190, https://doi.org/10.1038/s41377-024-01532-z.

70. S. E. Mann, E. M. Schooneveld, N. J. Rhodes, G. Mauri, D. Liu, and G. Jeff Sykora, "Nanoparticle ZnS:Ag/^{6}LiF—A New High Count Rate Neutron Scintillator with Pulse Shape Discrimination," *Journal of Physics D: Applied Physics* 57 (2024): 355301, https://doi.org/10.1088/1361-6463/ad5021.

Supporting Information

Additional supporting information can be found online in the Supporting Information section.

Supporting File: adfm74942-sup-0001-SuppMat.docx.

16163028, 0, Downloaded from https://advanced.onlinelibrary.wiley.com/doi/10.1002/adfm.74942 by Universita Milano Biococa, Wiley Online Library on [07/04/2026]. See the Terms and Conditions (https://onlinelibrary.wiley.com/terms-and-conditions) on Wiley Online Library for rules of use; OA articles are governed by the applicable Creative Commons License